Supplementary Information for

Ion-Cluster-Mediated Ultrafast Self-Healable Ionoconductors for Reconfigurable Electronics

Yong Min Kim,[1] Jin Han Kwon,[1] Seonho Kim,[2] U Hyeok Choi,[2] and Hong Chul Moon[1],*

[1]Department of Chemical Engineering, University of Seoul, Seoul 02504, Republic of Korea
[2]Department of Polymer Science and Engineering and Program in Environmental and Polymer Engineering, Inha University, Incheon 22212, Republic of Korea

*Corresponding author: H.C.M (hcmoon@uos.ac.kr)

This PDF file includes:

Supplementary Table 1 to 3

Supplementary Figure 1 to 26

Supplementary Reference 1 to 29

Other Supplementary Materials for this manuscript include the following :

Supplementary Movie 1 to 6

Supplementary Table 1 Molecular characterizations of polymers prepared in this work.

Code	M_w (g mol^{-1})[a]	M_n (g mol^{-1})[a]	Polydispersity index ($Đ$)[a]	Mole fraction of hydroxyl parts (%)[b]
100-AAHA	946,000	430,000	2.2	0
92-AAHA	1,274,000	490,000	2.6	8
61-AAHA	1,250,600	481,000	2.6	39
90-DAHA	898,700	473,000	1.9	10

[a]Measured by SEC with poly(ethylene oxide) standards; [b]Determined by ^{1}H NMR spectroscopy.

Supplementary Table 2 Comparison of healing mechanism, efficiency, temperature, and mechanical properties (Young's modulus and fracture strain) of previously reported self-healing platforms, including ionogels, hydrogels, and elastomers.

Materials	Type	Healing Mechanism	Healing Efficiency (%)	Healing Time (h)	Healing Temperature (°C)	Young's Modulus (MPa)	Fracture Strain (%)	Ref.
PAAm[a]/PNAGA[b]	Hydrogel	hydrogen bond	N.A.	0.5	90	0.048	665	1
UPyHCBA[c]	Hydrogel	hydrophobic interaction, hydrogen bond	N.A.	0.042	25	0.0017	1000	2
PAAc[d]/CTA[e]	Hydrogel	hydrophobic interaction	75	0.5	80	0.016	900	3
MPTC[f]/NaSS[g]/DMAEA[h]/BIS[i] copolymer	Hydrogel	electrostatic interaction	75	0.125	25	0.036	650[a]	4
P(NaSS-co-DMAEA-Q)	Hydrogel	electrostatic interaction	82.3	24	25	0.08	1000	5
Zwitterionic nanocomposite hydrogel	Hydrogel	electrostatic interaction	74	24	25	0.0046[x]	2000	6
Agel[j]−DCMC[k] hydrogel	Hydrogel	imine bond	90	1	37	0.03	140	7
P(AM-co-AEAM[l]) hydrogel	Hydrogel	hydrogen bond, ionic interaction, Schiff base bond	53	48	25	0.02[x]	1205	8
P(Urea-IL[m]-SPMA[n])	Hydrogel	electrostatic interaction, hydrogen bond	91	24	25	0.18	720	9
hyperbranched polyurethane (HPDU)	Elastomer	hydrogen bond	96.5	10	90	0.8[x]	3100	10
Dopamine acrylamide/butyl acrylate/Ca^{2+}	Elastomer	hydrogen bond, metal coordination	37	24	25	3.9	310	11
poly(AAm/ChCl[o]-co-MA[p]/ChCl)	Elastomer	hydrogen bond	91	72	20	0.1	450	12
polyurethane acrylate	Elastomer	disulfide bond hydrogen bond	95	12	80	0.5[x]	400	13
polyurethane (DA-PU)	Elastomer	hydrogen bond, donor-acceptor interaction	97	6.67	60	1.33[x]	1900	14
PU-HEDS[q]-400	Elastomer	hydrogen bond, disulfide bond	95.4	24	50	5.04	553	15
Fe-Hpdca[r]-PDMS	Elastomer	metal-ligand interaction	90.3	48	25	0.54	1700	16
cellulose nanocrystal/ [BMIM][HSO$_4$] composite	Ion gel	electrostatic interaction	90.3	24	25	0.016	620	17
PS[s]-b-P(DMAAm[t]-r-AAc)/[EMI][TFSI]	Ion gel	hydrogen bond	90	3	25	0.5[x]	400	18
TetraPEG-Ant[u] /[EMI][TFSI]	Ion gel	photoisomerization	66	10	150	0.007[x]	950	19
P(AzoMA-r-NIPAm)-b-PEO-b-P(AzoMA-r-NIPAm)[v]/[BMI][PF$_6$]	Ion gel	photoisomerization	81	64	36	0.02[x]	450	20

PVDF-*co*-HFP[w]-5545/[EMI][OTf]	Ion gel	ion-dipole interaction	100.3	6	50	0.10	1500	21
PVDF-*co*-HFP-5545/[EMI][TFSI]	Ion gel	ion-dipole interaction	99.1	24	50	0.21	2000	22
Cellulose/[BMI][Cl]	Ion gel	hydrogen bond	96	2	25	1[x]	60	23
92-AAHA-IL	**Ion gel**	**ion cluster**	**90.3** **98.7** **99.7**	**0.016 (1min)** **0.050 (3min)** **0.083 (5min)**	**25**	**0.84**	**1130**	**This work**

[a]PAAm: poly(acrylamide), [b]PNAGA: poly(*N*-acryloyl glycinamide), [c]UPyHCBA: 4-(6-(3-(6-methyl-4-oxo-1,4-dihydropyrimidin-2-yl)ureido)hexylcarbamoyloxy)butyl acrylate, [d]PAAc: poly(acrylic acid), [e]CTA: cetyltrimethylammonium, [f]MPTC: [3-(methacryloylamino)propyl]trimethylammonium chloride, [g]NaSS: sodium p-styrenesulfonate hydrate, [h]DMAEA: 2-(dimethylamino)-ethyl methacrylate, [i]BIS: N,N′-methylenebis(acrylamide), [j]Agel: amino-gelatin, [k]DCMC: dialdehyde carboxymethyl cellulose, [l]AEAM: 2-aminoethyl acrylamide hydrochloride, [m]Urea-IL: imidazolium-based ionic liquid (IL) monomers with urea groups, [n]SPMA: 3-sulfopropyl methacrylate potassium salt, [o]ChCl: choline chloride, [p]MA: maleic acid, [q]HEDS: 2,2'-hydroxy ethyldisulfide, [r]Hpdca: 2,6-pyridinedicarboxamide, [s]PS: poly(styrene), [t]DMAAm: N,N-dimethylacrylamide, [u]TetraPEG-Ant: tetra-arm poly(ethylene glycol)-anthracene, [v]P(AzoMA-*r*-NIPAm)-*b*-PEO-*b*-P(AzoMA-*r*-NIPAm): Poly(4-phenylazophenyl methacrylate-*random*-N-isopropylacrylamide)-*block*-poly(ethylene oxide)-*block*-P(4-phenylazophenyl methacrylate-*random*-N-isopropylacrylamide),[w]PVDF-*co*-HFP: Poly(vinylidene fluoride-*co*-hexafluoropropylene).[x]calculated from produced stress-strain curve.

Supplementary Table 3 Vogel-Fulcher-Tammann (VFT) temperature fitting parameters of temperature dependence of the α_2 process.
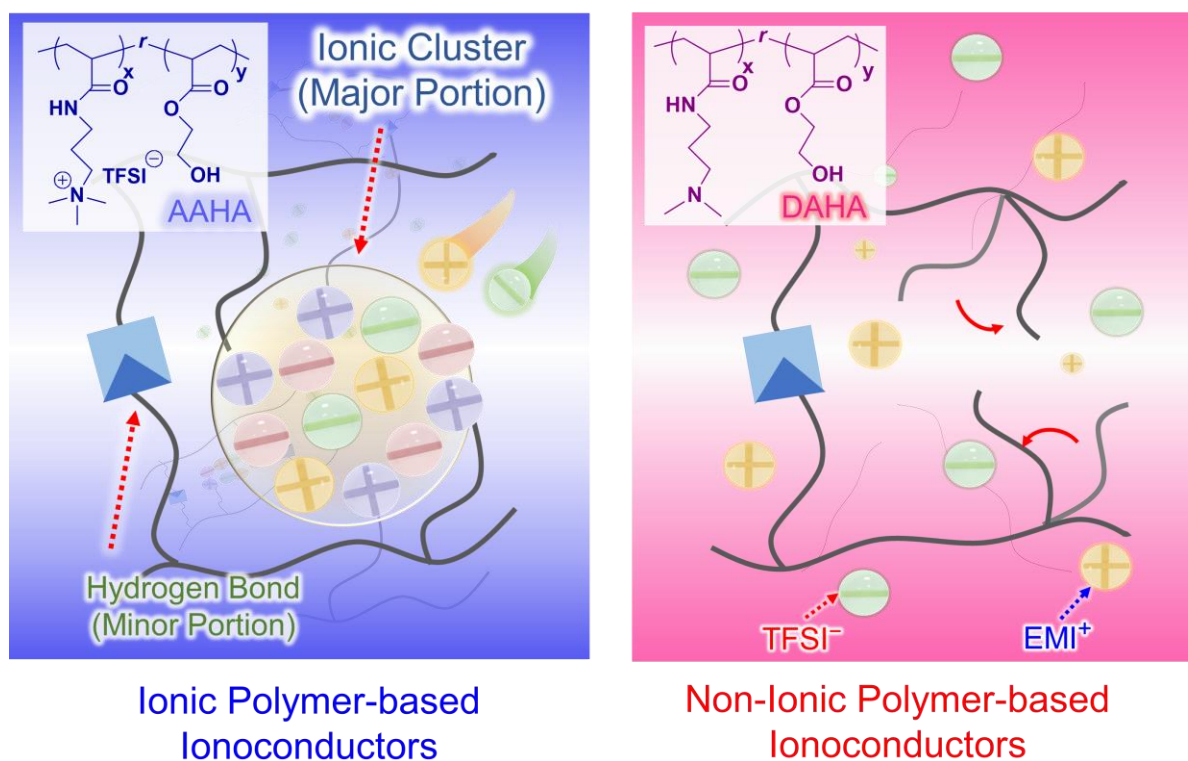
Sample	$\log(\omega_\infty)$ (rad s^{-1})	D	T_0 (K)	T_g[a] (K)	E_a (kJ/mol)
92-AAHA-IL	10.6	6	171	256	9
90-DAHA-IL	12.6	11	165	250	15

[a]Obtained from DSC thermograms (Supplementary Fig. 7).
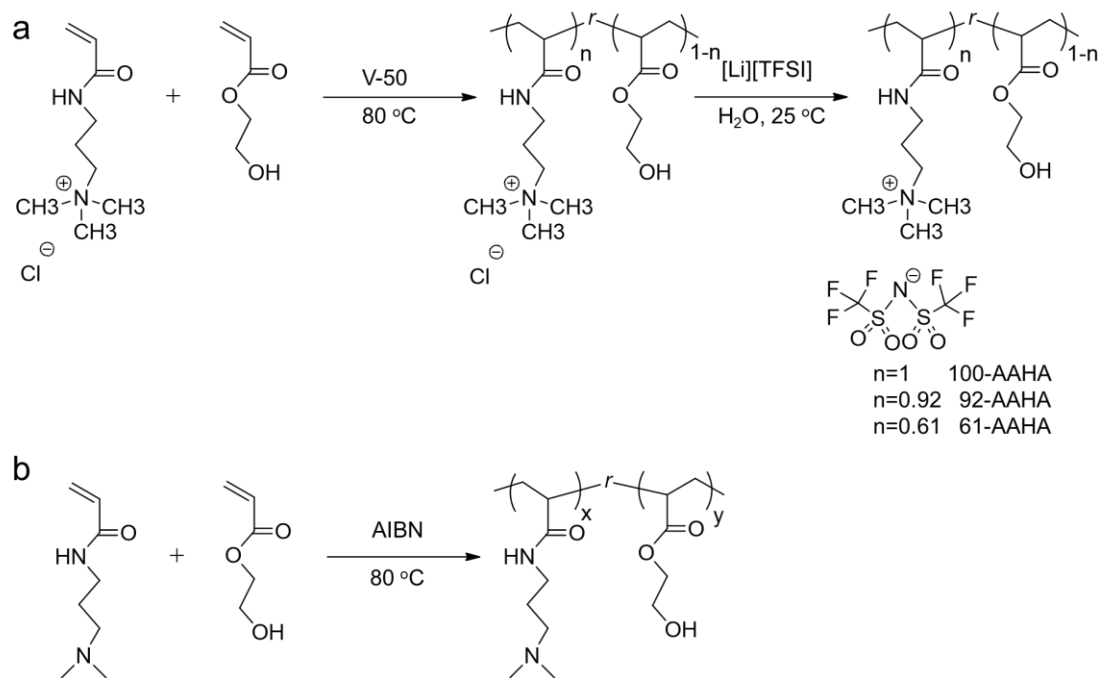
Supplementary Fig. 1 Synthetic strategy for copolymers employed in this work. Synthetic routes for preparing **a** AAHAs and **b** DAHA.

Supplementary Fig. 2 Difference in molecular interaction depending on the presence of ionic moiety. Schematic illustrations of ionic polymer-based ionoconductor (92-AAHA-IL), in which both hydrogen bonding and ion-cluster formation take place, and non-ionic polymer-based ionoconductors (90-DAHA-IL) only including hydrogen bonding interactions.
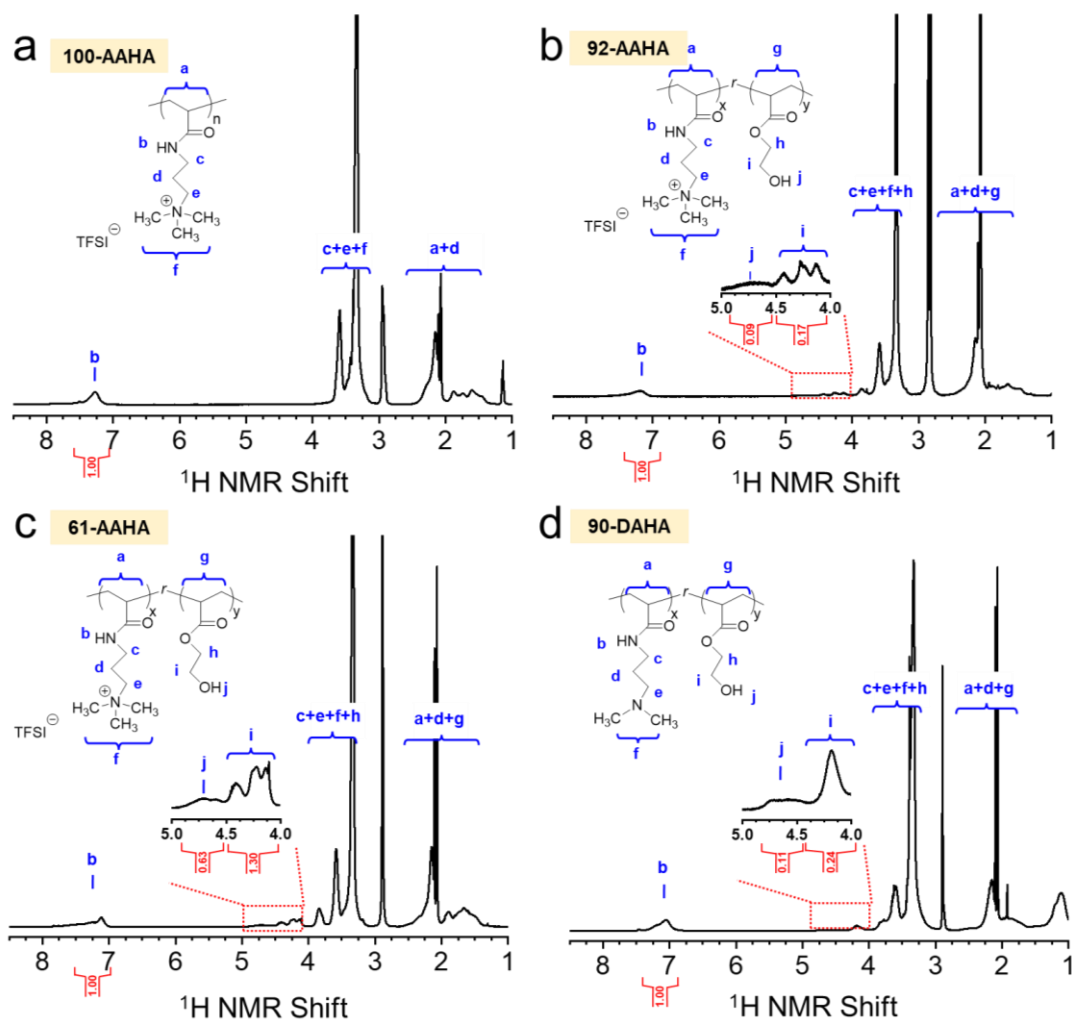
Supplementary Fig. 3 Structural analysis of used polymers. ^{1}H NMR spectra of prepared polymers. **a** 100-AAHA, **b** 92-AAHA, **c** 61-AAHA, and **d** 90-DAHA.
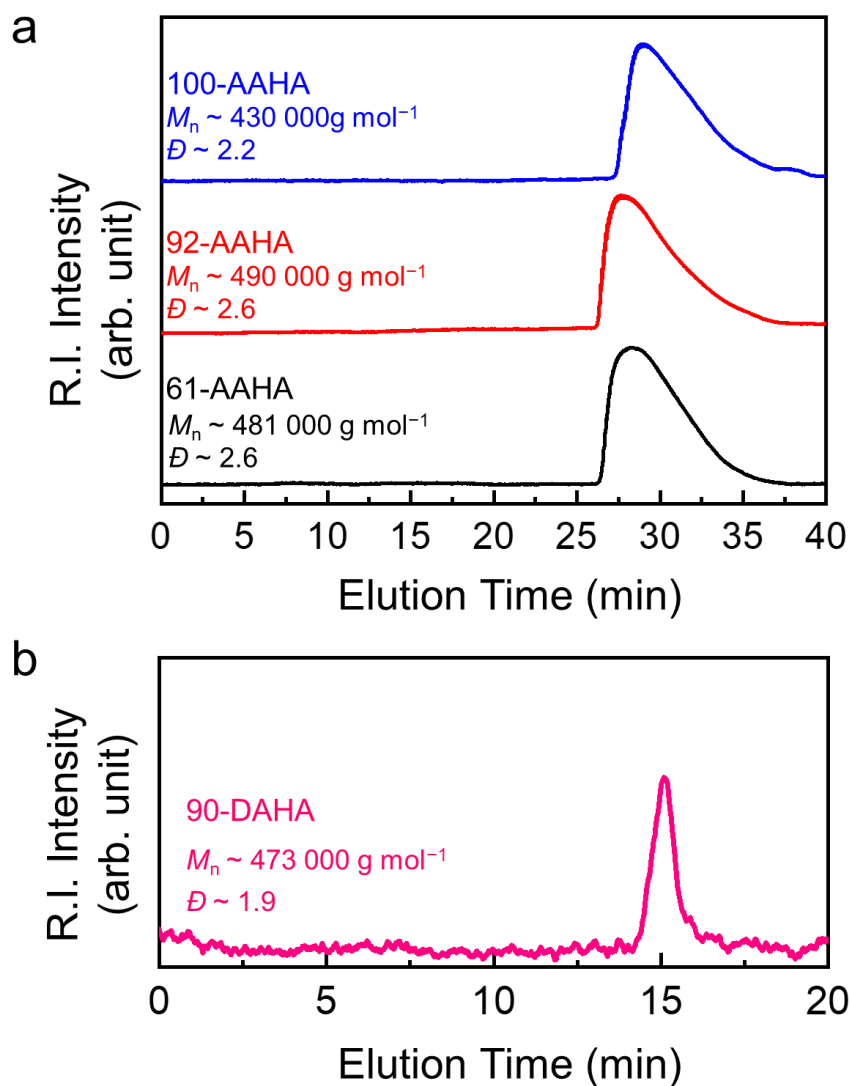
Supplementary Fig. 4 Molecular characteristics of used polymers. SEC traces of polymers employed in this study. **a** 100-AAHA, 92-AAHA, and 61-AAHA. To prepare the GPC samples, the synthesized AAHAs were dissolved in an aqueous buffer (pH = 3) containing 0.1 M sodium phosphate, and the operating flow rate was fixed at 0.5 mL min^{-1}. **b** SEC trace of 90-DAHA dissolved in HPLC water with a flow rate of 1.0 mL min^{-1}. All samples were calibrated with poly(ethylene oxide) standards.
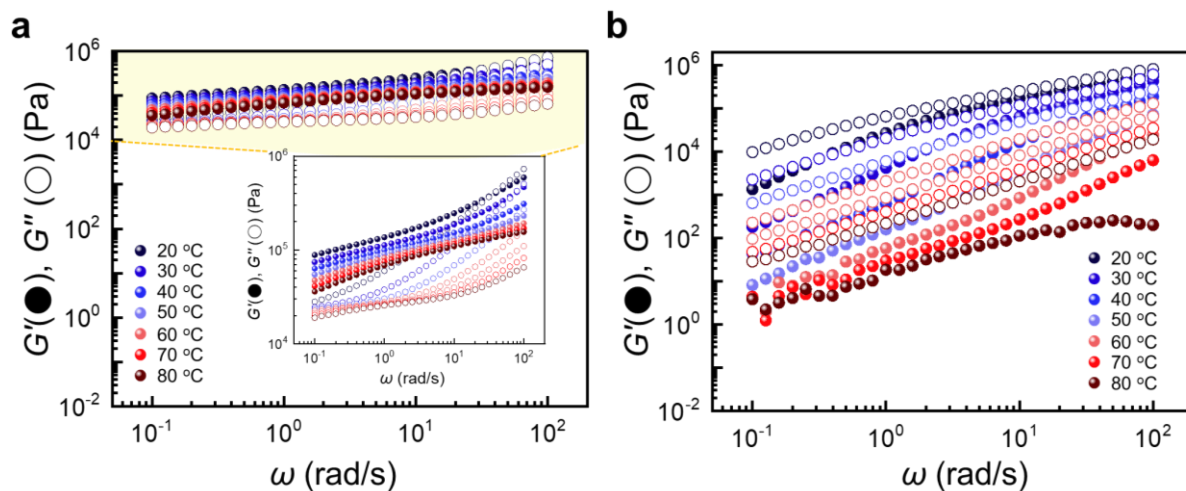
Supplementary Fig. 5 Difference in rheological behaviors. Frequency-dependent dynamic storage (filled circle) and loss (open circle) moduli at various temperatures for **a** 92-AAHA-IL and **b** 90-DAHA-IL.
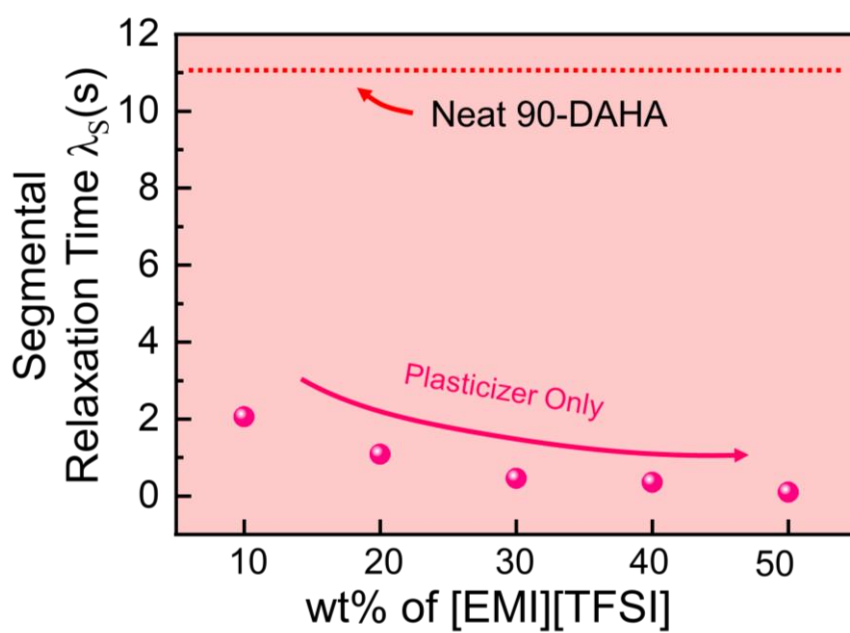
Supplementary Fig. 6 Effect of [EMI][TFSI] on non-ionic polymer-based system. Changes in segmental relaxation time of 90-DAHA-IL according to the weight fraction of the introduced [EMI][TFSI]. The red dotted-line indicates the segmental relaxation time of neat 90-DAHA.
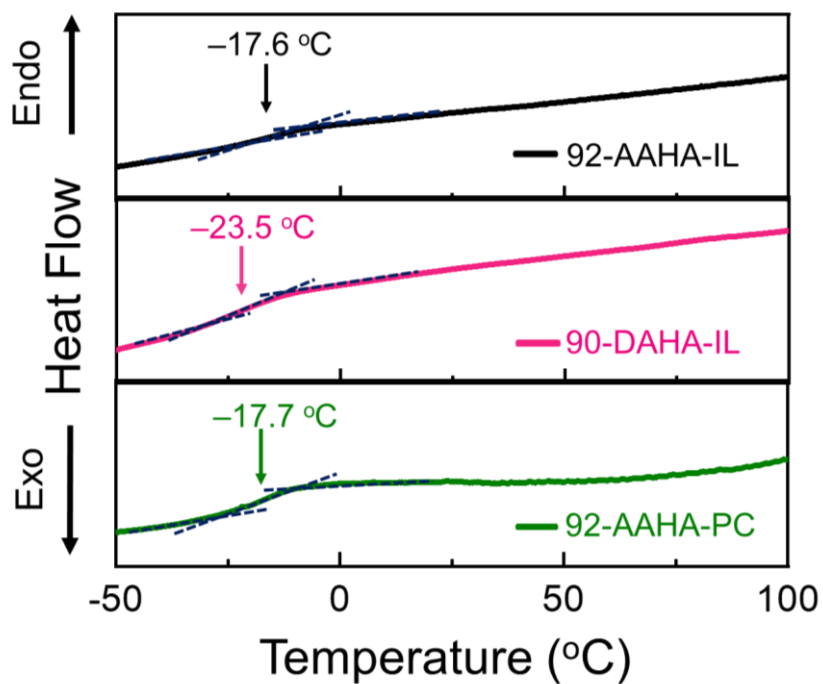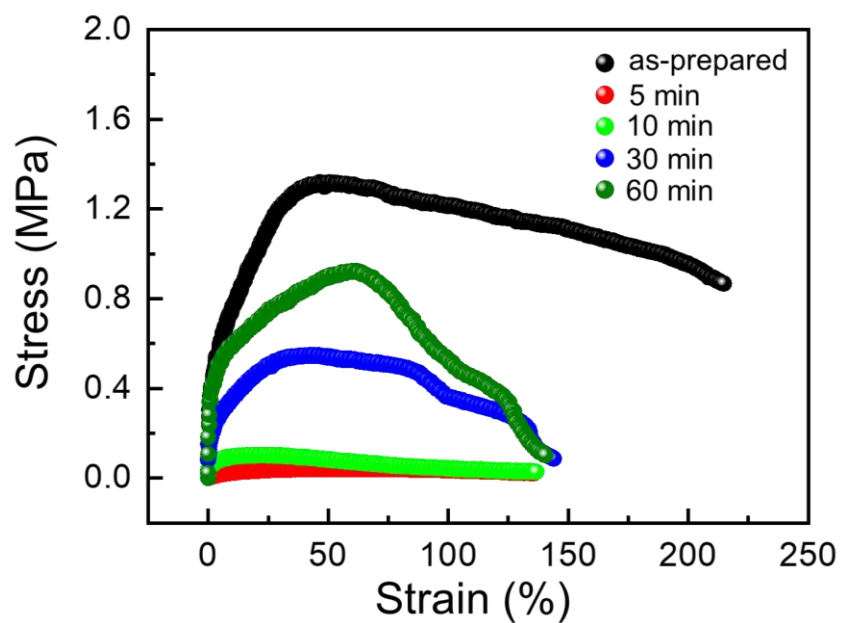
Supplementary Fig. 7 Thermal properties of various ionoconductors with different copolymers. DSC thermograms of 92-AAHA-IL, 90-DAHA-IL, and 92-AAHA-PC, obtained during the second run at a heating rate of 10 °C min^{-1}.
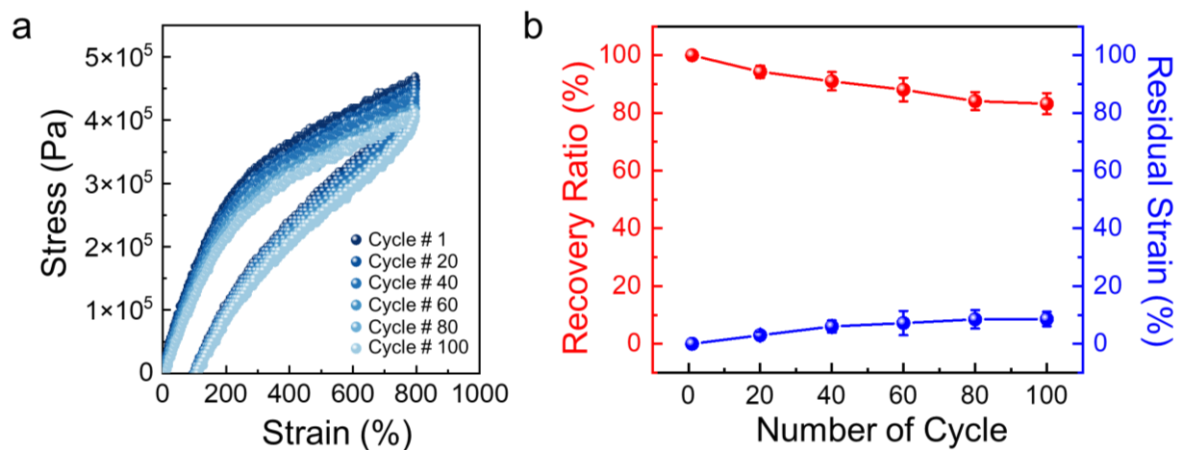
Supplementary Fig. 8 Mechanical stability of 92-AAHA-IL. a Stress-strain curves during cyclic stretching/releasing at 800% and **b** corresponding changes in recovery ratio and residual strain. The recovery ratio of ~83.2% and residual strain of ~8.6% after 100 consecutive cycles represent the high mechanical reliability of 92-AAHA-IL. Error bars indicate standard deviation.
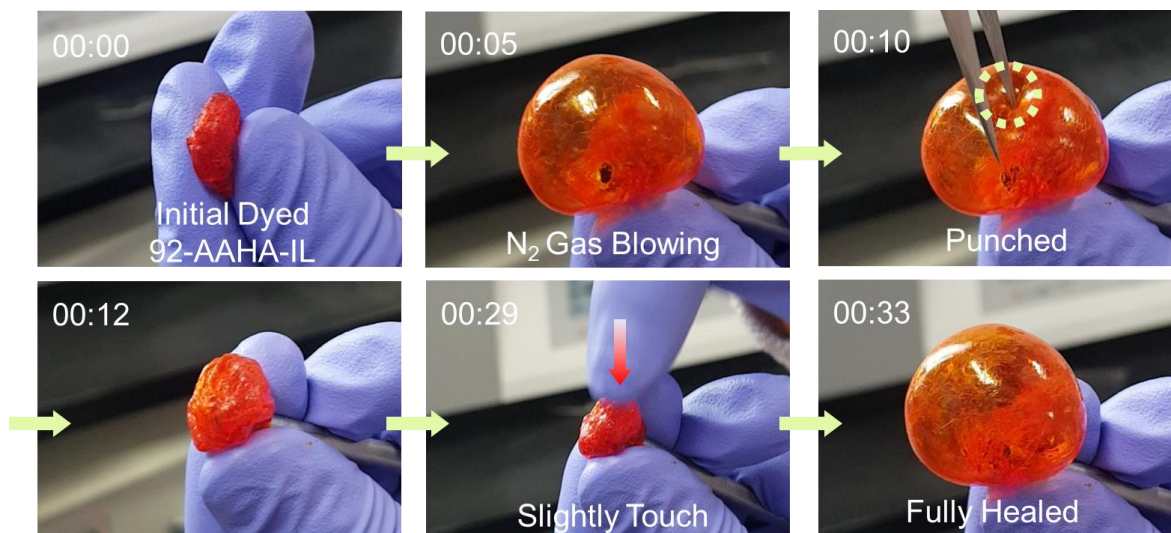
Supplementary Fig. 9 Demonstration of ultrafast self-healing performance of 92-AAHA-IL. Snapshots from Supplementary Movie 1 showing the immediate self-healing capability of 92-AAHA-IL. The balloon-shaped 92-AAHA-IL was expanded by blowing N_2 gas and punched with a tweezer to induce mechanical damage. After self-healing with a slight touch to contact the injured region, 92-AAHA-IL fully prevented the leakage of N_2 molecules.

Supplementary Fig. 10 Correlation between healing time and mechanical properties of 90-DAHA-IL. Tensile stress-strain curves of as-prepared and healed 90-DAHA-IL (5−60 mins) at 25°C.
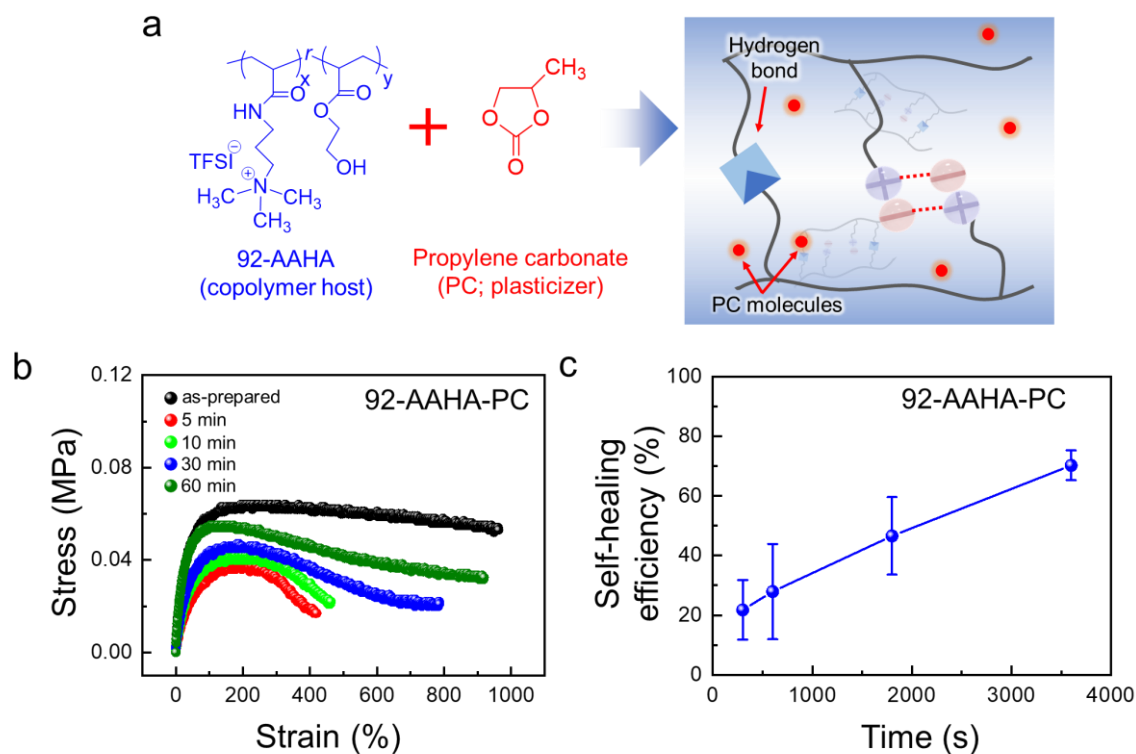
Supplementary Fig. 11 Mechanical and self-healing characteristics of the system with no ionic liquids. a Schematic illustration of 92-AAHA-PC. **b** Tensile stress–strain curves for self-healing tests of 92-AAHA-PC at 25 °C, and **c** self-healing efficiency as a function of healing time. The self-healing efficiency was calculated from the ratio of the toughness values before damage and after healing obtained from the stress–strain curves. Error bars indicate standard deviation.
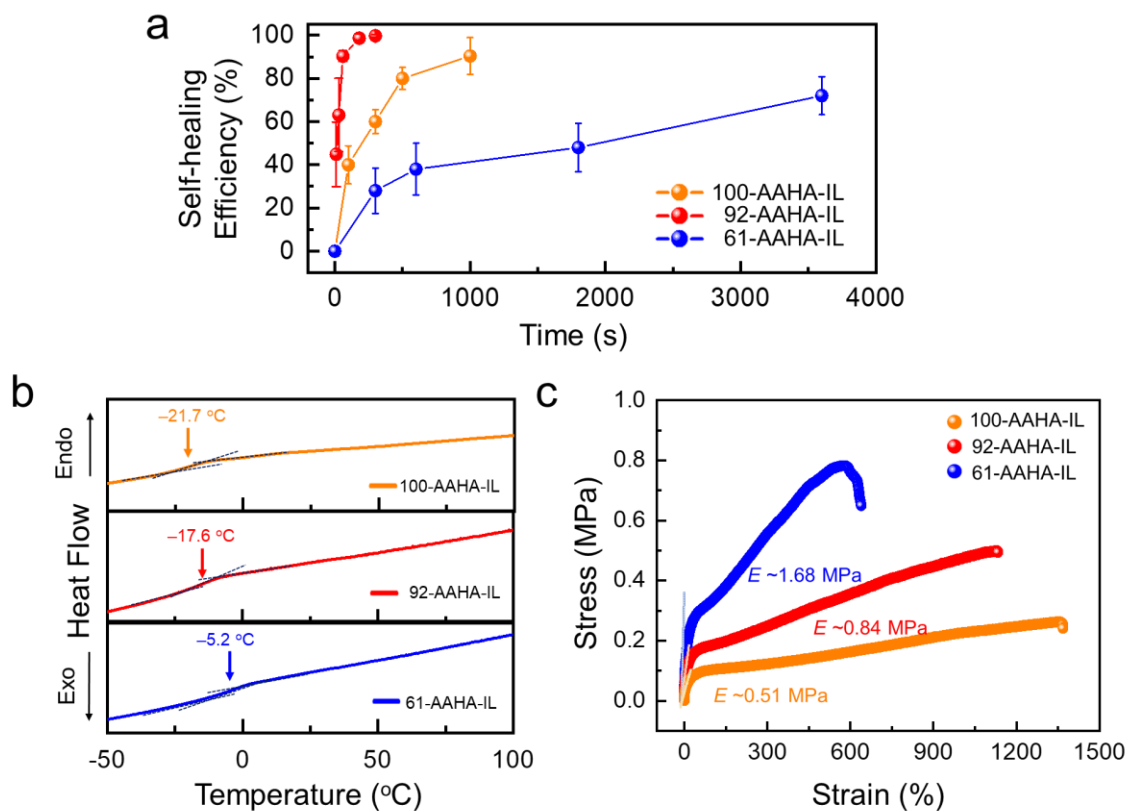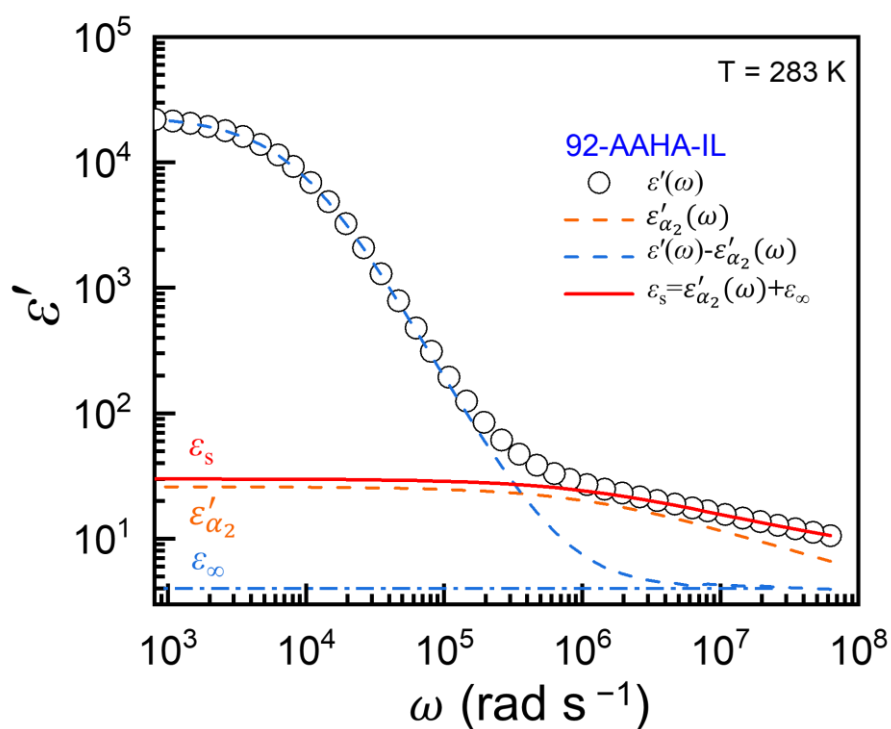
Supplementary Fig. 12 Dependence of self-healing, thermal, and mechanical performance on the ionic content in AAHA-IL. **a** Differences in self-healing efficiencies measured with different copolymer hosts. Error bars indicate standard deviation. **b** DSC thermograms for evaluating T_g values. **c** Tensile stress–strain curves for determining elastic moduli of 100-AAHA-IL, 92-AAHA-IL, and 61-AAHA-IL.
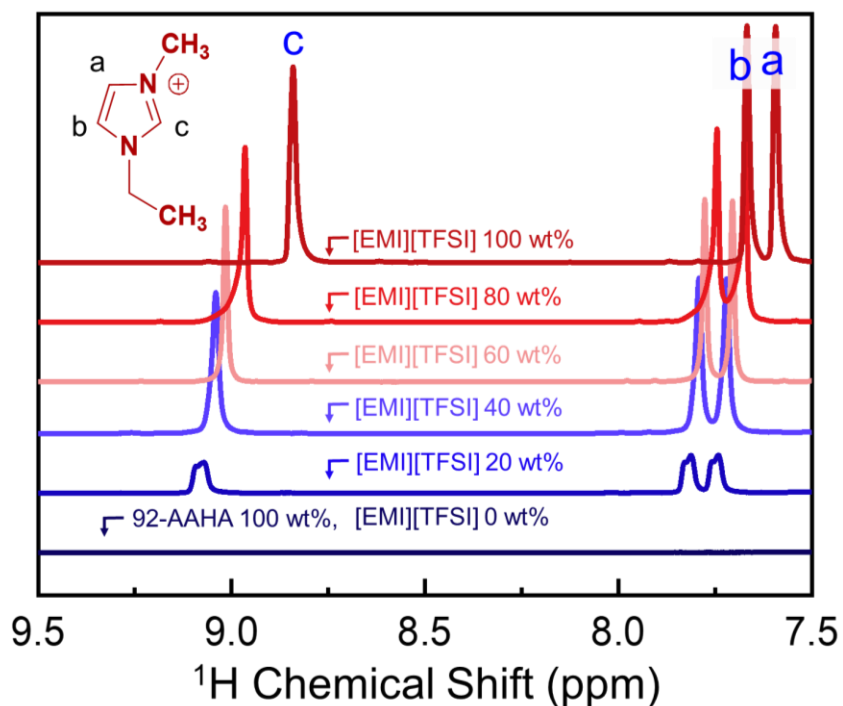
**Supplementary Fig. 13 Interaction between [EMI][TFSI] and 92-AAHA.** ^{1}H NMR spectra of [EMI][TFSI] with various 92-AAHA-IL contents. The contents of [EMI][TFSI] were 0 (navy line, neat 90-DAHA), 20, 40, 60, 80, and 100 wt.% (red line, neat [EMI][TFSI]). The representative [EMI]+ peaks were slightly shifted when the 92-AAHA was added, but no peaks below 7.5–9.5 ppm were observed for neat 92-AAHA.
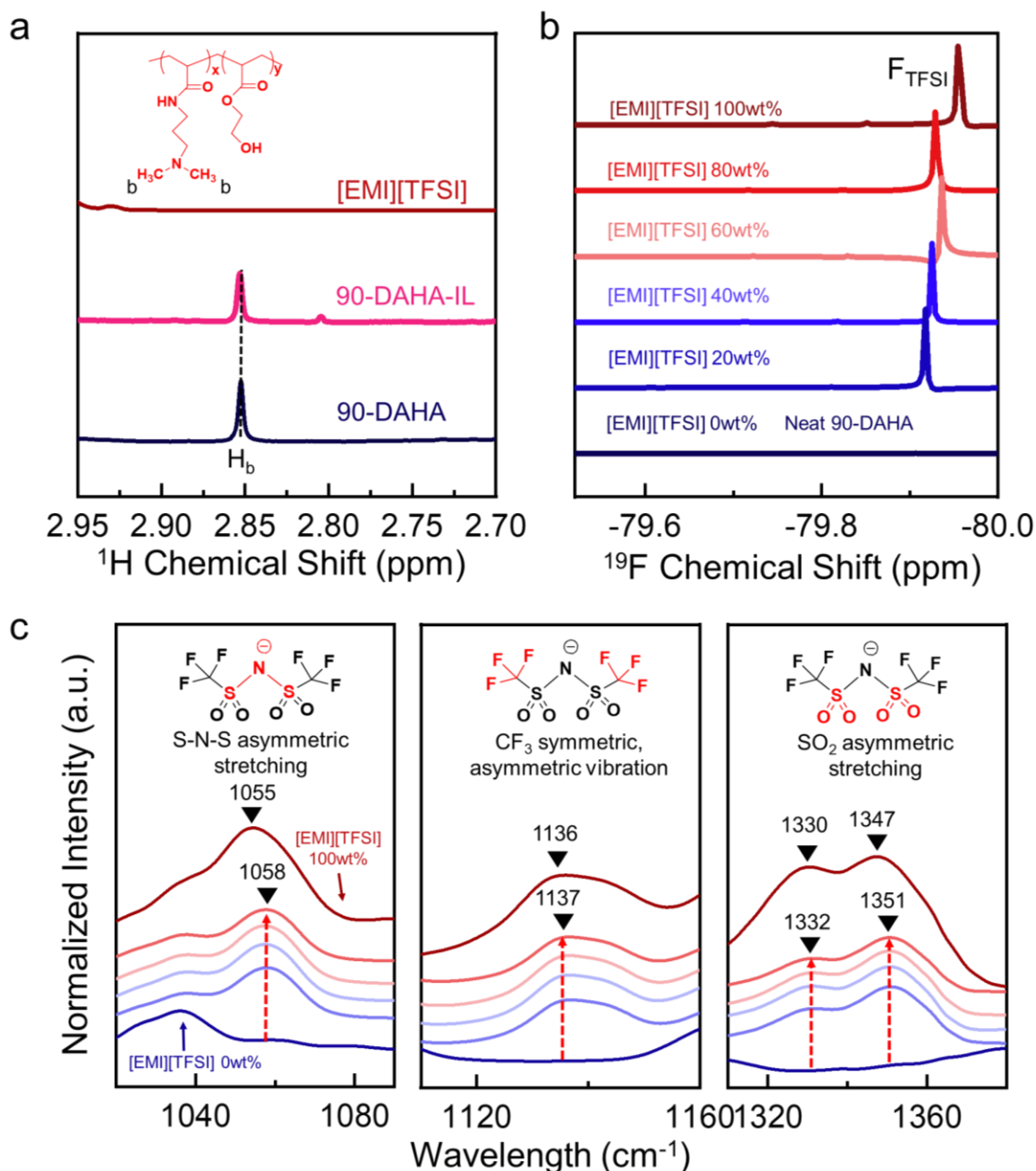
Supplementary Fig. 14 Spectroscopic analysis of 90-DAHA-containing system. a Comparison of ^{1}H NMR spectra of 90-DAHA, 90-DAHA-IL, and [EMI][TFSI]. 90-DAHA-IL contained 30 wt.% [EMI][TFSI]. **b** ^{19}F NMR spectra of 90-DAHA-IL with various [EMI][TFSI] contents. No [TFSI]$^-$ peak was observed for neat 90-DAHA. **c** Changes in FTIR absorption peaks with respect to the fraction of [TFSI]$^-$ in 90-DAHA-IL. The contents of [EMI][TFSI] were 0 (navy line, neat 90-DAHA), 20, 40, 60, 80, and 100 wt.% (red line, neat [EMI][TFSI]).

Supplementary Fig. 15 Frequency dependent dielectric characteristics of 92-AAHA-IL. Angular frequency dependence of dielectric permittivity $\varepsilon'(\omega)$ of 92-AAHA-IL at 283 K and corresponding static dielectric constant ε_s (red solid line), determined as the sum of the frequency-dependent contributions from the α_2 process $\varepsilon'_{\alpha_2}(\omega)$ (orange dashed line) and the high-frequency dielectric constant ε_∞ (blue dashed line).
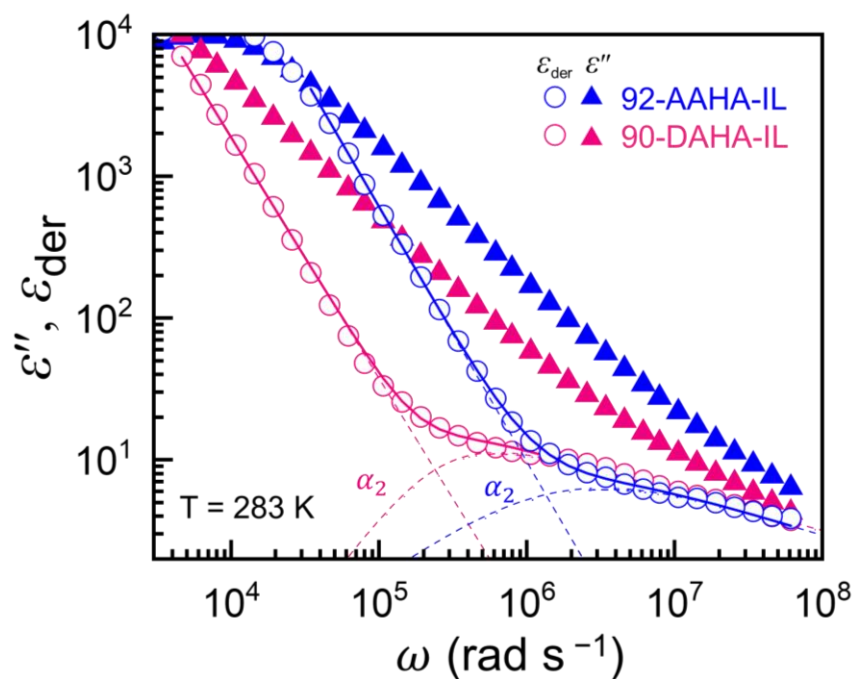
Supplementary Fig. 16 Different α_2 process between ionic- and non-ionic polymer-based ionoconductors. Derivative (open circles) and dielectric loss (filled triangles) spectra at 283 K and corresponding fits using a sum (solid line) of a power law for electrode polarization (dashed line) and a derivative form of the Havriliak-Negami function for the α_2 process (short dashed line).
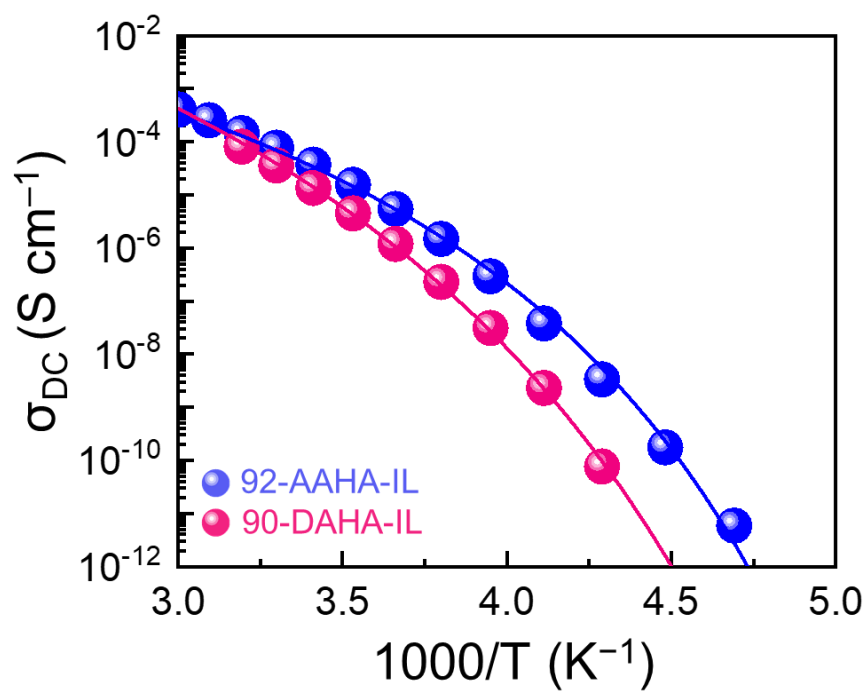
Supplementary Fig. 17 Temperature dependent ionic conductivity. Temperature dependence of ionic conductivity for 92-AAHA-IL and 90-DAHA-IL.
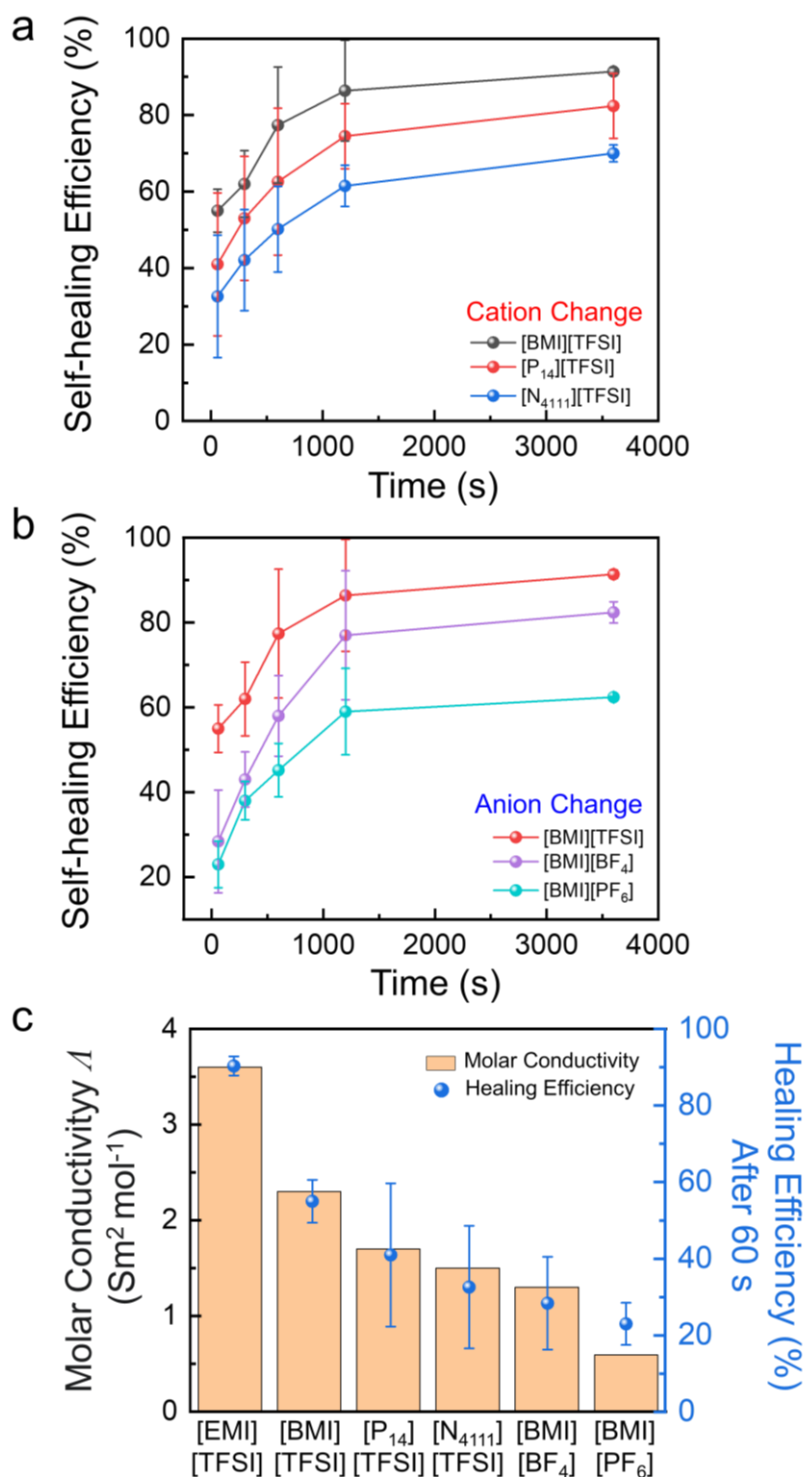
**Supplementary Fig. 18 Correlation between self-healing performance and type of ionic liquids.** Time-dependent self-healing efficiency of 92-AAHA-IL with selectively varied **a** cations and **b** anions of the ionic liquid. **c** Plots of molar conductivity (Λ) and healing efficiency of ionoconductors at a repair time of 60 s. The Λ values were extracted from ref. 24. The self-healing processes of all ionoconductors were performed at 25 °C. Considering that a higher Λ of ionic liquids indicates an easier ion–ion dissociation and ion movement, the superior performance of the [EMI][TFSI]-containing 92-AAHA-IL can be rationalized in terms of the highest Λ of the ionic liquid additive. All error bars indicate standard deviation.
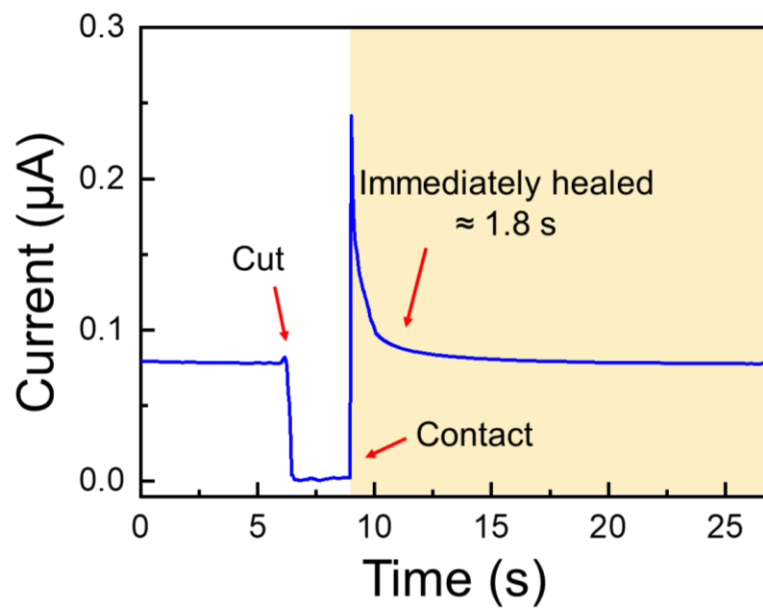
Supplementary Fig. 19 Self-healing effect on electrical properties. Self-healing of electrical properties of 92-AAHA-IL film. The flowing current was turned off when the film was cut in half, and was recovered immediately (~1.8 s) after reconnection.
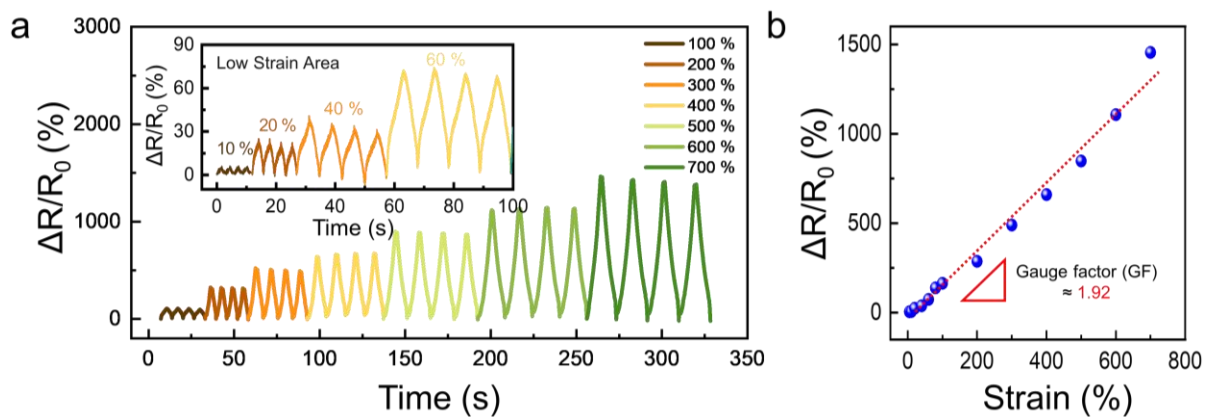
Supplementary Fig. 20 Sensory performance of 92-AAHA-IL. a Relative resistance variations ($\Delta R/R_0$) under applied strains up to 700% (inset: relative resistance changes at 10, 20, 40, and 60% strains). **b** Variations in $\Delta R/R_0$ over extended strain range, from which a GF value of ~1.92 was extracted. It should be noted that the ionoconductors alone can serve as ionic sensing platforms with no additional components. Accordingly, strain-sensing platforms can be readily fabricated by simply connecting electronic wires.
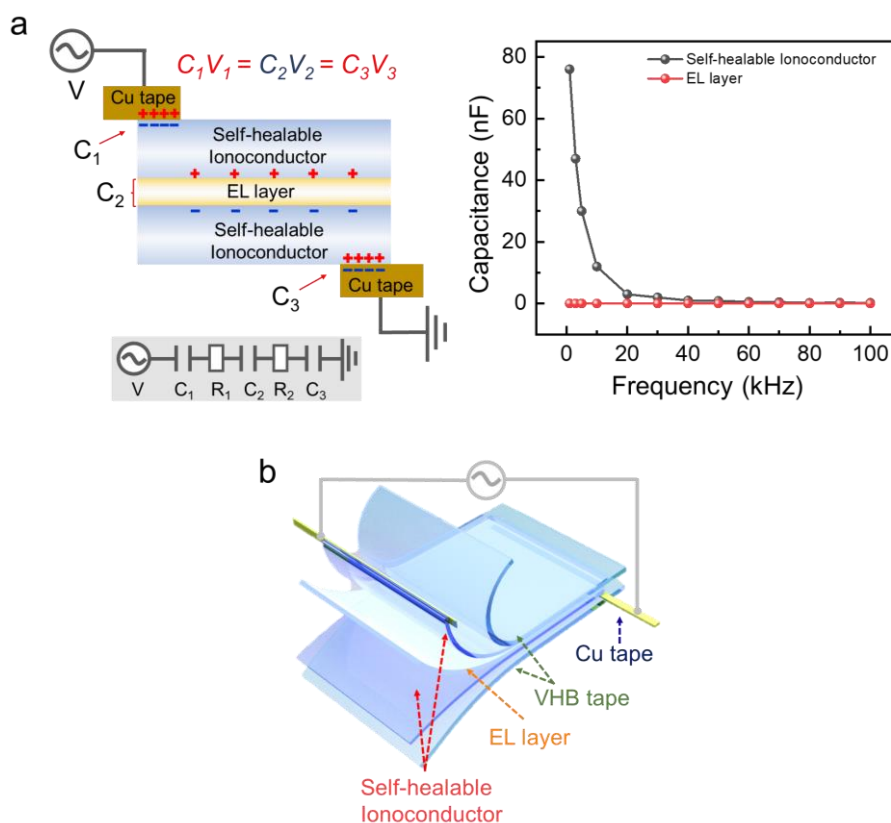
Supplementary Fig. 21 Application of 92-AAHA-IL in AC electroluminescent displays (ACEDs). a Schematic diagram (left) of ACED and capacitance variations (right) of each component (EL layer and 92-AAHA-IL-based ionoconductor). To construct electrical double layers (EDLs), Cu tape was attached to both sides of the ionoconductor. To avoid unnecessary interfacial electrochemical reactions, the EDL area (A_{EDL}) was a small portion of the total area of the ionoconductor (A_{Ion}). The EDL and dielectric layer acted as a series capacitor, following the equation: $Q = C_1V_1 = C_2V_2 = C_3V_3$, where Q is the charge, while C and V represent the corresponding capacitance and voltage of each layer, respectively.[25,26] Accordingly, the EL layer had a relatively lower capacitance than the EDLs in ionoconductors in a lower frequency range (0.1 to 60 kHz), and the applied voltage was centered on the phosphor layer (C_1/C_2 or $C_3/C_2 \approx 1.8 \times 10^4$). **b** Schematic illustration of ACED. The EL device had a three-layer configuration where the EL phosphor layer was sandwiched between two symmetric ionoconductor layers.
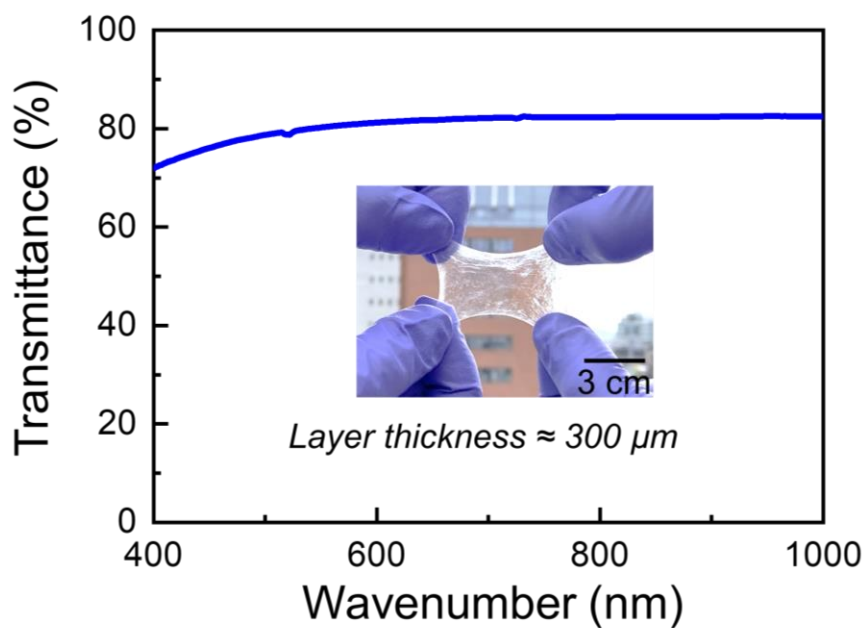
Supplementary Fig. 22 Optical transparency of 92-AAHA-IL. Transmittance spectrum of 300 μm-thick 92-AAHA-IL film at various wavenumbers. The overall transmittance values were higher than ~70 % at 400–1100 nm.
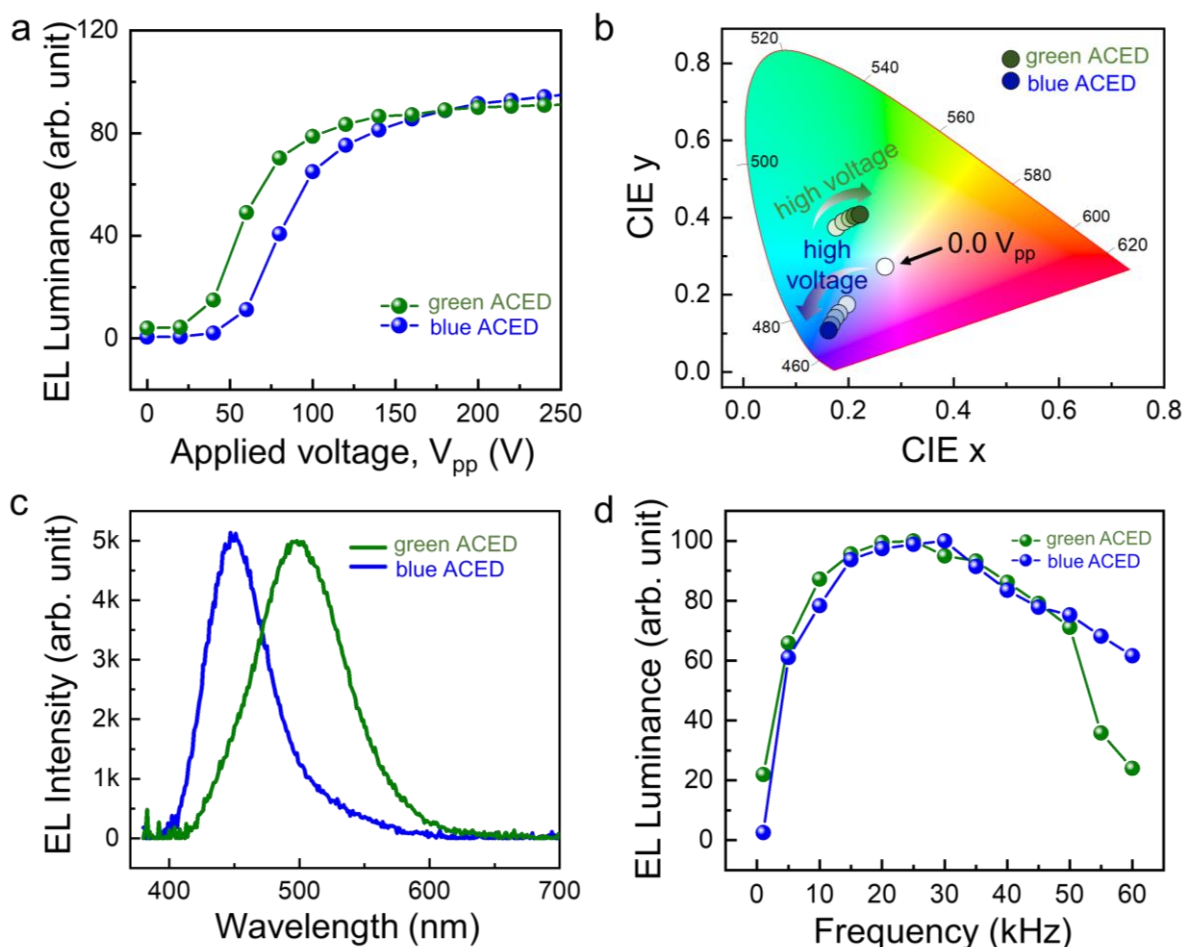
Supplementary Fig. 23 Characteristics of AC electroluminescent displays (ACEDs). a Luminance *versus* voltage characteristics and **b** CIE color coordinates of blue- and green-emitting ACED as a function of AC voltage at a frequency of 25 kHz. **c** EL emission spectra and **d** frequency dependence of EL luminance at an applied voltage of 200 V_{pp}. The magnitude of the emission intensity was linearly related to the driving voltage power from the turn-on voltage (~40 V_{pp}) to the saturation of both EL brightness above 200 V_{pp} (Supplementary Fig. 23a). Each green- and blue-emitting luminophore successfully served as a deep color-brightening ACED upon applying various voltages (Supplementary Fig. 23b). The normalized EL spectra of the ACEDs confirmed the blue and green emission with maximum EL wavelengths at ~450 and ~500 nm (Supplementary Fig. 23c). The analysis of the frequency dependence showed that the EL intensity rapidly increased up to 25 kHz at the applied voltage of 200 V_{pp} (Supplementary Fig. 23d). However, further frequency increases (above 30 kHz) resulted in a steady reduction in luminance, due to the decrease in the electron acceleration.[27] Therefore, the operating conditions of ACEDs were optimized at an applied voltage of 200 V_{pp} and a frequency of 25 kHz to synchronize the green- and blue-emitting systems.
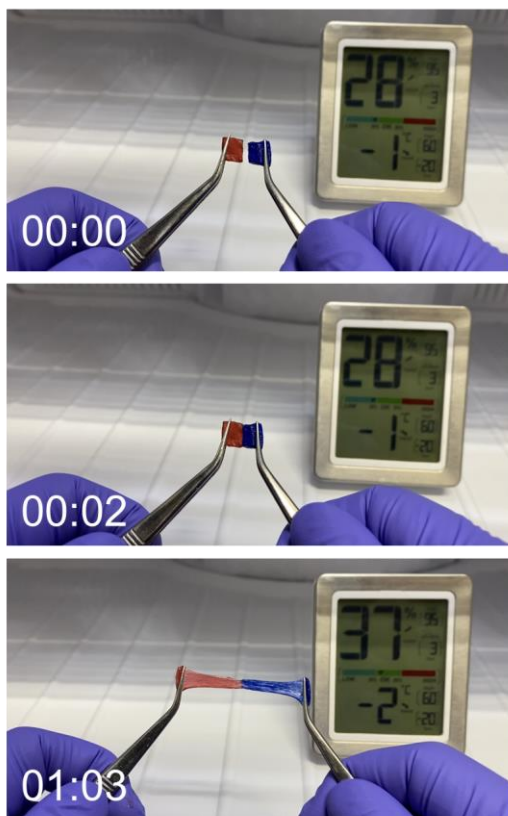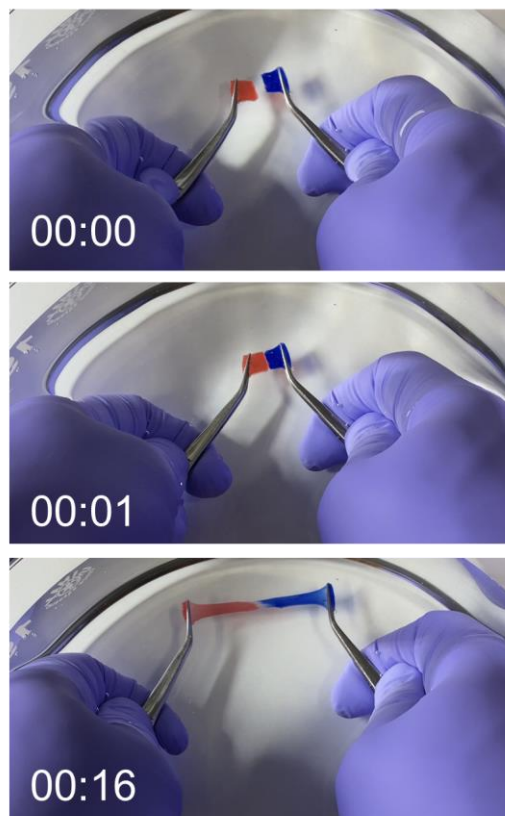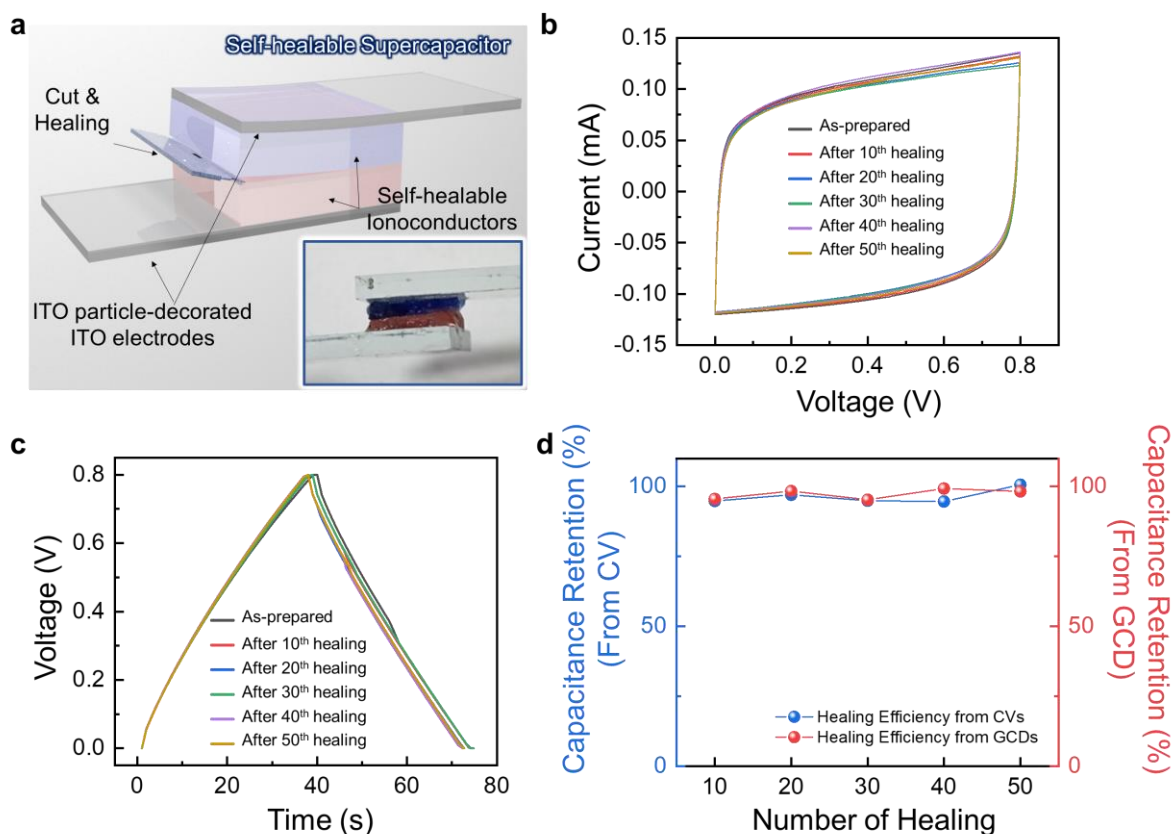
Supplementary Fig. 24 Successful self-healing in various conditions. Successful self-healing of 92-AAHA-IL in extreme environments: **a** sub-zero temperature and **b** underwater environment.
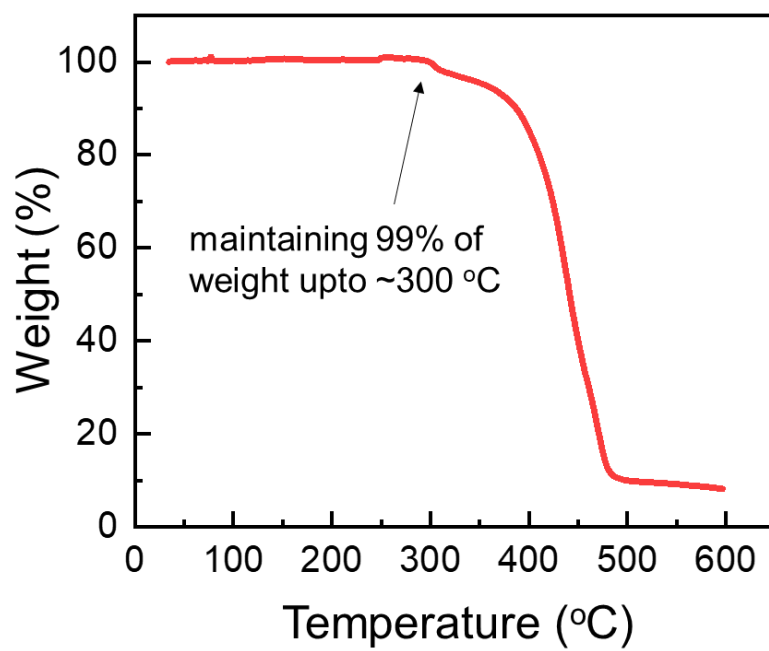
Supplementary Fig. 25 Thermal stability of 92-AAHA-IL. TGA thermogram of 92-AAHA-IL, indicating its high thermal stability up to ~300 ℃.

Supplementary Fig. 26 Utilization of ultrafast self-healing performance of 92-AAHA-IL in healable supercapacitors. **a** Schematic illustration of self-healable ionoconductor-based electrical double layer capacitor (EDLC). The inset displays a photograph of the actual device. **b** Cyclic voltammograms at a scan rate of $25\,\mathrm{mV\,s^{-1}}$ during self-healing cycles. The areal capacitance (C) was calculated using the following equation:[28] $C = \frac{1}{\Delta V(dV/dt)} \int I\, dV$, where dV/dt and $\int I\, dV$ are the voltage scan rate and the numerical integration of the current density in the half-cycle potential window (ΔV), respectively. **c** Galvanostatic charge-discharge (GCD) profiles at a current density of $0.1\,\mathrm{mA\,cm^{-2}}$. The C values were extracted using the equation[29] $C = I\Delta t/S\Delta V$, where I, Δt, S, and ΔV represent the discharging current, discharging time, electrode area, and potential window excluding the IR voltage drop, respectively. **d** Variation in capacitance retention (C/C_0) as a function of number of healing cycles. A high C/C_0 was maintained irrespective of the number of self-healing cycles, demonstrating the practical applicability of 92-AAHA-IL in self-healable energy storage devices.

Supplementary References

[1] Dai, X. et al. A mechanically strong, highly stable, thermoplastic, and self-healable supramolecular polymer hydrogel. *Adv. Mater.* **27**, 3566–3571 (2015).

[2] Jeon, I. et al. Extremely stretchable and fast self-healing hydrogels. *Adv. Mater.* **28**, 4678–4683 (2016).

[3] Gulyuz, U. et al. Self-healing poly(acrylic acid) hydrogels with shape memory behavior of high mechanical strength. *Macromolecules* **47**, 6889–6899 (2014).

[4] Zhang, Y. et al. Unique self-reinforcing and rapid self-healing polyampholyte hydrogels with a pH-induced shape memory effect. *Macromolecules* **54**, 5218–5228 (2021).

[5] Ihsan, A. B. et al. Self-healing behaviors of tough polyampholyte hydrogels. *Macromolecules* **49**, 4245−4252 (2016).

[6] Wang, L. et al. Tough, adhesive, self-healable, and transparent ionically conductive zwitterionic nanocomposite hydrogels as skin strain sensors. *ACS Appl. Mater. Interfaces* **11**, 3506–3515 (2019).

[7] Lei, J. et al. Facile fabrication of biocompatible gelatin-based self-healing hydrogels. *ACS Appl. Polym. Mater.* **1**, 1350−1358 (2019).

[8] Wu, M. et al. Ultra elastic, stretchable, self-healing conductive hydrogels with tunable optical properties for highly sensitive soft electronic sensors. *J. Mater. Chem. A* **8**, 24718–24733 (2020).

[9] Long, T. et al. Salt-mediated polyampholyte hydrogels with high mechanical strength, excellent self-healing property, and satisfactory electrical conductivity. *Adv. Funct. Mater.* **28**, 1804416 (2018).

[10] Chen, X. et al. Extremely tough, puncture-resistant, transparent, and photoluminescent polyurethane elastomers for crack self-diagnose and healing tracking. *ACS Appl. Mater. Interfaces* **12**, 30847−30855 (2020).

[11] Li, J. et al. Seawater-assisted self-healing of catechol polymers via hydrogen bonding and coordination interactions. *ACS Appl. Mater. Interfaces* **8**, 19047−19053 (2016).

[12] Li, R. et al. Autonomous self-healing, antifreezing, and transparent conductive elastomers. *Chem. mater.* **32**, 874−881 (2020).

[13] Li, X. et al. Self-healing polyurethane elastomers based on a disulfide bond by digital light processing 3D printing. *ACS Macro Lett.* **8**, 1511−1516 (2019).

[14] Ying, W. B. et al. A biologically muscle-inspired polyurethane with super-tough, thermal reparable and self-healing capabilities for stretchable electronics. *Adv. Funct. Mater.* **31**, 2009869 (2021).

[15] Xu, W. M. et al. Sunlight driven self-healing, reshaping and recycling of a robust, transparent and yellowing-resistant polymer. *J. Mater. Chem. A* **4**, 10683–10690 (2016).

[16] Li, C.-H. et al. A highly stretchable autonomous self-healing elastomer. *Nat. Chem.* **8**, 618–624 (2016).

[17] Zhu, M. et al. Long-lasting sustainable self-healing ion gel with triple-network by trigger-free dynamic hydrogen bonds and ion bonds. *ACS Sustain. Chem. Eng.* **6**, 17087−17098 (2018).

[18] Tamate, R. et al. Self-healing micellar ion gels based on multiple hydrogen bonding. *Adv. Mater.* **30**, 1802792 (2018).

[19] Saruwatari, A. et al. Photohealable ion gels based on the reversible dimerisation of anthracene. *Chem. Commun.* **54**, 13371−13374 (2018).

[20] Ueki, T. et al. Thermally reversible ion gels with photohealing properties based on triblock copolymer self-assembly. *Macromolecules* **48**, 5928−5933 (2015).

[21] Cao, Y. et al. A transparent, self-healing, highly stretchable ionic conductor. *Adv. Mater.* **29**, 1605099 (2017).

[22] Cao, Y. et al. Self-healing electronic skins for aquatic environments. *Nat. Electron.* **2**, 75–82 (2019).

[23] Zhao, D. et al. A dynamic gel with reversible and tunable topological networks and performances. *Matter* **2**, 390−403 (2020).

[24] Tokuda, H. et al. How ionic are room-temperature ionic liquids? an indicator of the physicochemical properties. *J. Phys. Chem. B* **110**, 19593–19600 (2006).

[25] Wang, J. et al. Extremely stretchable electroluminescent devices with ionic conductors. *Adv. Mater.* **28**, 4490–4496 (2016).

[26] Xuan, H. D. et al. Super stretchable and durable electroluminescent devices based on double-network ionogels. *Adv. Mater.* **33**, 2008849 (2021).

[27] Liang, G. et al. Self-healable electroluminescent devices. *Light-Sci. Appl.* **7**, 102 (2018).

[28] Allagui, A. et al. Reevaluation of Performance of Electric Double-layer Capacitors from Constant-current Charge/Discharge and Cyclic Voltammetry. *Sci. Rep. 6,* 38568 (2016).

[29] Kim, S. Y. et al. Reliable, high-performance electrochromic supercapacitors based on metal-doped nickel oxide. *ACS Appl. Mater. Interfaces* **12**, 51978-51986 (2020).